



CHORUS

This is the accepted manuscript made available via CHORUS. The article has been published as:

Band-gap engineering of rutile-structured SnO_2 - GeO_2 - SiO_2 alloy system

Hitoshi Takane, Yuichi Ota, Takeru Wakamatsu, Tsutomu Araki, Katsuhisa Tanaka, and Kentaro Kaneko

Phys. Rev. Materials **6**, 084604 — Published 26 August 2022

DOI: [10.1103/PhysRevMaterials.6.084604](https://doi.org/10.1103/PhysRevMaterials.6.084604)

Bandgap engineering of rutile-structured SnO₂-GeO₂-SiO₂ alloy system

Hitoshi Takane^{1,2 a)}, Yuichi Ota³, Takeru Wakamatsu¹, Tsutomu Araki⁴, Katsuhisa Tanaka¹ and Kentaro Kaneko^{2,5,6,7 a)}

¹*Department of Material Chemistry, Kyoto University, Kyoto 615-8510, Japan*

²*Department of Electronic Science and Engineering, Kyoto University, Kyoto 615-8510, Japan*

³*Tokyo Metropolitan Industrial Technology Research Institute, Tokyo 135-0064, Japan*

⁴*Department of Electrical and Electronic Engineering, Ritsumeikan University, Shiga 525-8577, Japan*

⁵*Engineering Education Research Center, Kyoto University, Kyoto 615-8530, Japan*

⁶*Photonics and Electronics Science and Engineering Center, Kyoto University, Kyoto 615-8520, Japan*

⁷*Research Organization of Science and Technology, Ritsumeikan University, Shiga 525-8577, Japan*

^{a)} Author to whom correspondence should be addressed: takane.hitoshi.33v@st.kyoto-u.ac.jp, ken0710@fc.ritsumei.ac.jp

Abstract

Rutile-structured germanium oxide (r-GeO₂), a novel ultra-wide bandgap semiconductor, is a promising candidate for future high-power electronics because of its excellent properties, including ambipolar dopability, high carrier mobilities, and a higher thermal conductivity than β -Ga₂O₃. In this work, focusing on a wide variety of its applications, we propose an ultra-wide bandgap alloy system based on r-GeO₂ and other rutile-structured oxides (SnO₂-GeO₂-SiO₂), and clarify the electronic structure and electrical properties based on the experiments and the first-principles calculations. Experimentally, (001)-oriented r-Ge_xSn_{1-x}O₂ alloy thin films with an entire range of Ge compositions (x) were grown by a mist chemical vapor deposition technique. Structural characterizations show that the fabricated r-Ge_xSn_{1-x}O₂ alloy films with $x \leq 0.96$ and the well-crystallized part of the film with $x = 1.00$ have uniform chemical compositions and the same epitaxial relations with r-TiO₂ (001) substrates. Transmission electron microscopy observations reveal that there are few dislocations in r-Ge_{0.66}Sn_{0.34}O₂ because of relatively small in-plane lattice mismatch. In contrast, a large number of dislocations are observed near the film/substrate interface in r-Ge_{0.96}Sn_{0.04}O₂. Lattice constants of the alloys both along the a - and c -axis decrease with increase in Ge compositions. Their bandgaps were determined by spectroscopic ellipsometry analysis, indicating that the bandgaps increase as Ge compositions increase (3.81–4.44 eV) with a bowing parameter of 1.2 eV. The values of lattice constants and the trend of bandgaps transition obtained by calculations are in good agreement with those of experimentally obtained each other. Then, we presented the calculated natural band alignments of r-Ge_xSn_{1-x}O₂ and r-Ge_xSi_{1-x}O₂ alloys, suggesting possibility of p-type doping in r-GeO₂ and Ge-rich r-Ge_xSn_{1-x}O₂, and availability of r-SiO₂ and Si-rich r-Ge_xSi_{1-x}O₂ as a blocking layer of other rutile-structured devices. Finally, electrical measurements demonstrated n-type conductivities in r-Ge_xSn_{1-x}O₂ ($x \leq 0.57$).

1. Introduction

Increasing demands for energy-saving societies have raised attentions to ultra-wide bandgap (UWBG) semiconductors, with a bandgap (E_g) larger than 3.4 eV, as advanced materials for high-power and radio-frequency (RF) electronic devices as well as deep-UV optoelectronic devices¹. For example, β -Ga₂O₃ ($E_g=4.48\text{--}4.9$ eV)^{2,3} is one of the most investigated UWBG materials due to the availability of its substrate as well as its large breakdown field. However, conventional UWBG materials including β -Ga₂O₃ have difficulties in effective ambipolar doping and conduction, which restricts full use of themselves for various applications.

Now, there is a great interest in rutile-structured germanium oxide (r-GeO₂), with $E_g=4.44\text{--}4.68$ eV⁴⁻⁶ comparable to β -Ga₂O₃, because it is theoretically and experimentally reported that r-GeO₂ has ambipolar dopability^{5,7}, high carrier mobility ($\mu_e=244$ cm²V⁻¹s⁻¹ ($\perp c$) and 377 cm²V⁻¹s⁻¹ ($\parallel c$), $\mu_h=27$ cm²V⁻¹s⁻¹ ($\perp c$) and 29 cm²V⁻¹s⁻¹ ($\parallel c$))⁸, large breakdown field (7.0 MVcm⁻¹)⁸, and higher thermal conductivity (51 Wm⁻¹K⁻¹) than β -Ga₂O₃ (11–27 Wm⁻¹K⁻¹)⁹. Moreover, bulk r-GeO₂ can be grown¹⁰⁻¹², indicating that homoepitaxial growth of r-GeO₂ will be possible in the future. Recently, growth of r-GeO₂ thin film has also been reported¹³⁻¹⁵.

Considering a wide variety of its applications, establishment of an alloy system based on r-GeO₂, like III-V semiconductors¹⁶, III-group nitrides^{17,18}, and corundum-structured oxides^{19,20}, is important because alloy semiconductors are bases for heterostructure contributing to various optical and electrical devices. In Fig. 1 (a) and (b), we propose a novel ultra-wide bandgap alloy system composed of rutile-structured oxides (GeO₂-SnO₂-SiO₂ and TiO₂). r-SnO₂, which possesses a bandgap of 3.56 eV²¹ and an unintentional n-type conductivity, has been studied as an attractive material for transparent conductive oxides (TCOs)²², sensors^{23,24}, transistors^{25,26}. r-SiO₂, also known as stishovite, a high-pressure phase of SiO₂, was reported to have an extremely large bandgap of 8.75 eV²⁷. r-TiO₂, with a bandgap of 3.03 eV²⁸, shows n-type conductivity by Nb- or Ta-doping. For device-oriented researches, fabrication of its alloy thin films and evaluation of their physical and structural properties are needed. In particular, modulation of bandgaps, lattice parameters, and electrical properties by changing alloy compositions is important for applications in heterostructure devices such as high electron mobility transistors (HEMT),

heterojunction bipolar transistors (HBT).

In this work, we report comprehensive studies of $r\text{-Ge}_x\text{Sn}_{1-x}\text{O}_2$ alloy thin films with an entire range of Ge compositions (x). Experimentally, we performed structural characterization, bandgap modulation, and the analysis of electrical properties. Along with the experiments, we carried out the first-principles calculations based on density functional theory (DFT) for detailed clarification of crystal and electronic structures. Then, the discussion is extended to the perspective of the $\text{GeO}_2\text{-SnO}_2\text{-SiO}_2$ alloy system based on the calculations.

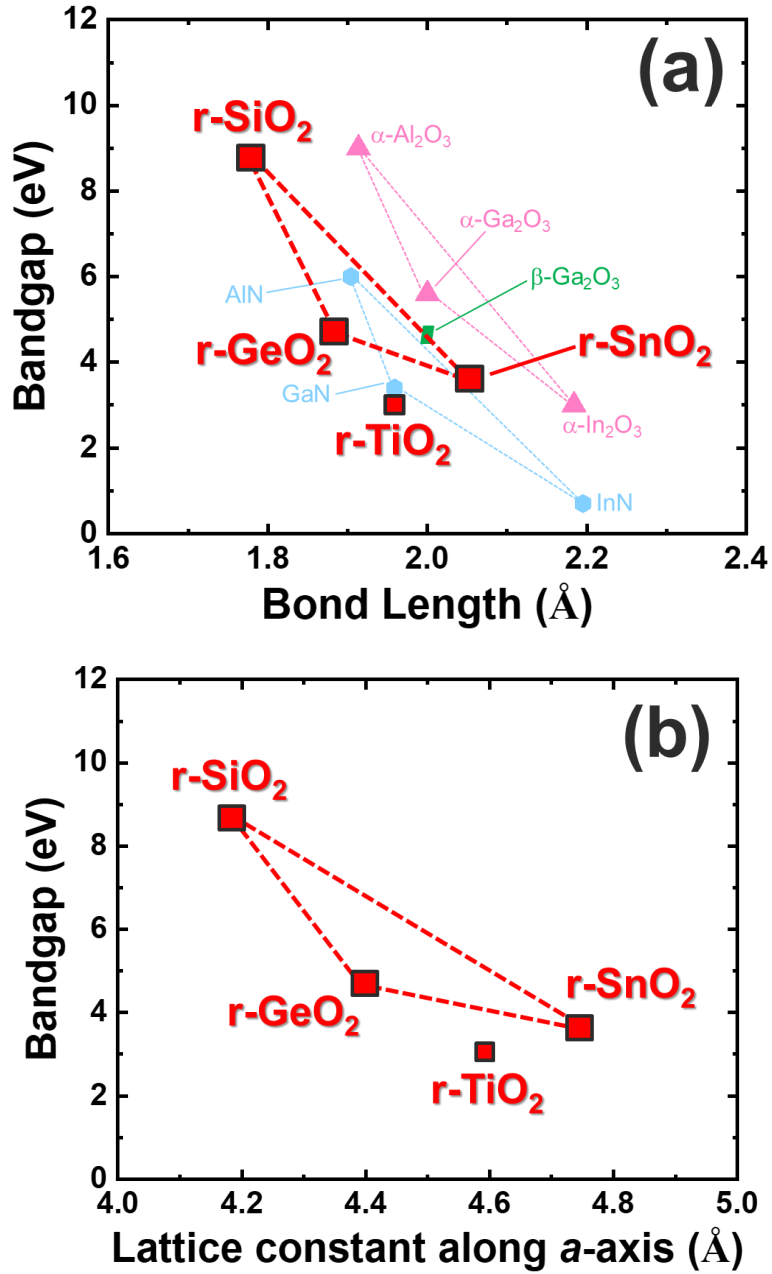


Fig. 1 (a) Relationships between band gap and bond length of a new alloy system based on rutile-structured oxides (r-GeO₂, r-SnO₂, r-SiO₂, r-TiO₂)^{4,21,27-29}. Those of conventional ones (III-group nitrides and corundum-structured oxides) and β-Ga₂O₃ are also presented³⁰. (b) Relationship between band gap and lattice constant along *a*-axis of the alloy system.

2. Experimental

$r\text{-Ge}_x\text{Sn}_{1-x}\text{O}_2$ alloy thin films were grown on $r\text{-TiO}_2$ (001) substrates by a mist chemical vapor deposition (mist CVD) technique. Table 1 shows the common growth recipe for $r\text{-Ge}_x\text{Sn}_{1-x}\text{O}_2$ alloy thin films. Bis [2-carboxyethylgermanium (IV)] sesquioxide (Tokyo Chemical Industry Co., Ltd.) and tin (II) chloride dihydrate (FUJIFILM Wako Pure Chemical Corp.) were used as germanium and tin precursors, respectively. We dissolved them in deionized water (H_2O) with addition of a small amount of hydrochloric acid (HCl), which helped to solve the precursors completely. For the growth of $r\text{-Ge}_x\text{Sn}_{1-x}\text{O}_2$ alloy thin films with different solidus compositions of Ge (x), we used a mixed solution of the two precursors with different Ge concentration ratios in the source solutions. The growth temperature was fixed at 725 °C and both carrier and dilution gases were O_2 with flow rate of 3.0 L/min and 0.5 L/min, respectively. Detailed growth conditions (growth time, concentration of Ge and Sn in the source solution) for each $r\text{-Ge}_x\text{Sn}_{1-x}\text{O}_2$ alloy thin film are listed in Table 2. In addition, in the mist CVD setup of this work, we used two different quartz tubes, where the atomized source solution flows and growth reaction occurs. That is, we used quartz tubes with different length (50 and 75 cm), because required time to decompose Sn and Ge precursors is considered to be different. In order to extend decomposition time for Ge precursor, we used the quartz tube with the length of 75 cm for the growth of $r\text{-Ge}_{0.96}\text{Sn}_{0.04}\text{O}_2$ and GeO_2 film, similarly to Ref. 14. Note that all the samples in this work were fabricated without intentional doping. The crystal structures of the $r\text{-Ge}_x\text{Sn}_{1-x}\text{O}_2$ were evaluated by X-ray diffraction (XRD) measurements using $\text{Cu K}\alpha_1$ radiation with a primary Ge monochromator (Rigaku, ATX-G). The microstructure of the $r\text{-Ge}_x\text{Sn}_{1-x}\text{O}_2$ was observed by transmission electron microscopy (TEM) with acceleration voltage of 120 kV (FEI TECNAI F20X). The surface morphologies of the $r\text{-Ge}_x\text{Sn}_{1-x}\text{O}_2$ films were observed by scanning electron microscopy (SEM) with acceleration voltage of 15 kV (Hitachi High-Tech, TM4000Plus). Energy dispersive X-ray spectroscopy (EDS) and electron backscatter diffraction (EBSD) measurement (Oxford Instruments, AZtecOne) were conducted to characterize the chemical compositions and crystallographic orientation in the $r\text{-Ge}_x\text{Sn}_{1-x}\text{O}_2$. Their bandgaps were determined by spectroscopic ellipsometry (SE) analysis in the photon energy range of 1.5-6.5 eV (wavelength range of 190-826 nm) and at incidence angles of 70 ° (HORIBA, Ltd., UVISEL). Finally, their electrical properties were acquired

by the four-probe method and Hall effect measurements with DC magnetic field (TOYO Corp., ResiTest 8340). For the electrical measurements, we evaporated Ti (30 nm)/Au (50 nm) electrode on the sample surface with the van der Pauw configuration.

Table 1 Common growth recipe for $r\text{-Ge}_x\text{Sn}_{1-x}\text{O}_2$ alloy thin films.

Ge precursor	bis [2-carboxyethylgermanium (IV)] sesquioxide: $\text{C}_6\text{H}_{10}\text{Ge}_2\text{O}_7$
Sn precursor	tin (II) chloride dihydrate: $\text{SnCl}_2 \cdot 2\text{H}_2\text{O}$
Solvent	$\text{H}_2\text{O} + \text{HCl}$
Substrate	r-TiO ₂ (001)
Carrier gas (Flow rate)	O ₂ (3.0 L/min)
Dilution gas (Flow rate)	O ₂ (0.5 L/min)
Growth temperature	725 °C

Table 2 Detailed growth conditions for each of the $r\text{-Ge}_x\text{Sn}_{1-x}\text{O}_2$ alloy thin films.

Ge compositions (x)	Growth time (min)	$\text{C}_6\text{H}_{10}\text{Ge}_2\text{O}_7$ in solution (m mol/L)	$\text{SnCl}_2 \cdot 2\text{H}_2\text{O}$ in solution (m mol/L)	Quartz tube length (cm)
0.00	30	0	50	50
0.41	15	16	25	50
0.57	15	16	16	50
0.66	15	13	6	50
0.70	60	5	2.5	50
0.96	30	10	2.5	75
1.00	25	10	0	75

3. Calculation

We performed the first-principles calculations based on the DFT by using Quantum ESPRESSO (QE) package^{31,32} and Wien2k code³³. For r-Ge_xSn_{1-x}O₂ and r-Ge_xSi_{1-x}O₂ alloys modeling, we employed a generalized special quasi-random structure (SQS) generated by USPEX code³⁴⁻³⁶ which include 48 atoms per cell ($2 \times 2 \times 2$ primitive unit cell structure) and 6 atoms per cell ($1 \times 1 \times 1$ primitive unit cell structure) for the alloys and the end members (GeO₂, SiO₂, and SnO₂), respectively. The structure optimization was performed by Perdew–Burke–Ernzerhof functional revised for solids (PBEsol)³⁷ with the QE package. We adopted Ge, Sn, Si, and O pseudopotential files from standard solid-state pseudopotential (SSSP) libraries.³⁸ The kinetic energy cutoff for wavefunctions of 80 Rydberg (Ry) and a charge density cutoff of 650 Ry, respectively, and $6 \times 6 \times 10$ and $10 \times 10 \times 16$ k points grid were used for the alloys and the end of members, respectively.³⁹ After structure optimization, the self-consistent calculations were performed by Wien2k code with 400 and 1000 k points sampling for the alloys and the end of members, respectively, PBE⁴⁰ functional and $R_a K_{max} = 7.0$, where R_a is the smallest muffin-tin radius (here is about 1.6–1.7 a.u. for each alloys) and K_{max} gives the magnitude of the largest K vector in the plane-wave expansion. The band gap (E_g) calculations were also performed with the Tran–Blaha modified Becke Johnson (TB-mBJ)^{41,42} exchange potential implemented in Wien2k.

To determine the natural band edge positions of r-Ge_xSn_{1-x}O₂ and r-Ge_xSi_{1-x}O₂ alloys, we used atomic solid-state energy (SSE) scale method⁴³. The scheme requires the SSE values for constitute atoms and the bandgap of the system. We used the following SSE of absolute values for O, Ge, Si, and Sn: 7.96, 2.40, 2.37, and 4.26 eV, respectively⁴⁴. The bandgap values of r-Ge_xSn_{1-x}O₂ and r-Ge_xSi_{1-x}O₂ alloys were determined from calculations via cost-effectively TB-mBJ results.

4. Results and Discussions

A. Structural analysis by XRD and TEM

Figs. 2 (a) and (b) show XRD symmetric $2\theta/\omega$ scan profiles of $r\text{-Ge}_x\text{Sn}_{1-x}\text{O}_2$ alloy films on $r\text{-TiO}_2$ (001) substrate in a wide ($20\text{--}90^\circ$) and a narrow ($54\text{--}68^\circ$) range, respectively. The peaks of $r\text{-Ge}_x\text{Sn}_{1-x}\text{O}_2$ 002 diffraction and $r\text{-TiO}_2$ 002 diffraction are visible, indicating that (001)-oriented $r\text{-Ge}_x\text{Sn}_{1-x}\text{O}_2$ alloy films were grown on $r\text{-TiO}_2$ (001) substrates. Using the EDS described in detail later, Ge compositions (x) in each film were found to be 0.00, 0.41, 0.57, 0.66, 0.70, 0.96, and 1.00. The EDS compositions were calibrated by using standard samples, where metallic Sn and Ge powder were mixed with different compositions. It should be noted that the diffraction peak at around 30° in the profile for $x=0.70$ is considered to be attributed to a forbidden 001 diffraction by the film or substrate.

Fig. 2 (b) presents the XRD (301) Φ scan profile of the $r\text{-Ge}_{0.57}\text{Sn}_{0.43}\text{O}_2$ film on $r\text{-TiO}_2$ substrate. For the $r\text{-Ge}_{0.57}\text{Sn}_{0.43}\text{O}_2$ film, peaks appear at the same fourfold rotational angle Φ as (001) $r\text{-TiO}_2$ substrate with 90° interval. This suggests that (001)-oriented $r\text{-GeO}_2$ film was epitaxially grown on (001) TiO_2 substrate without rotational domains.

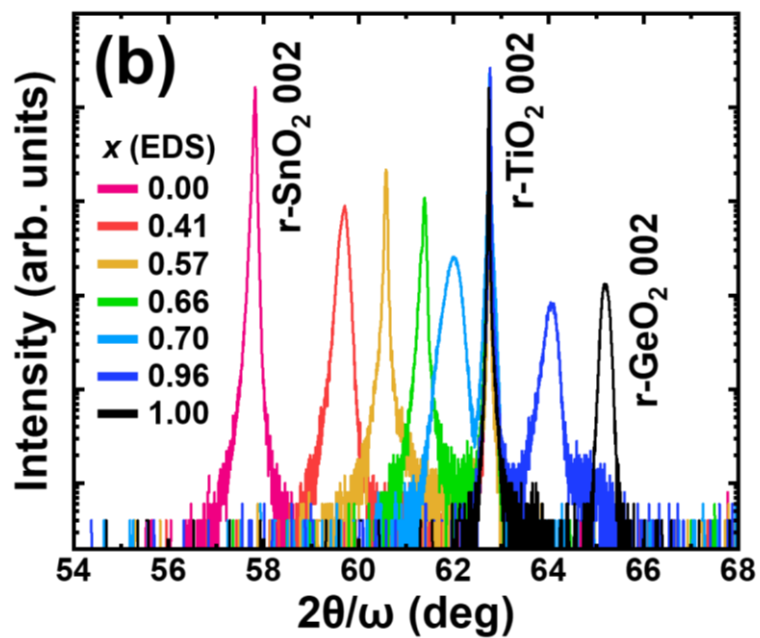
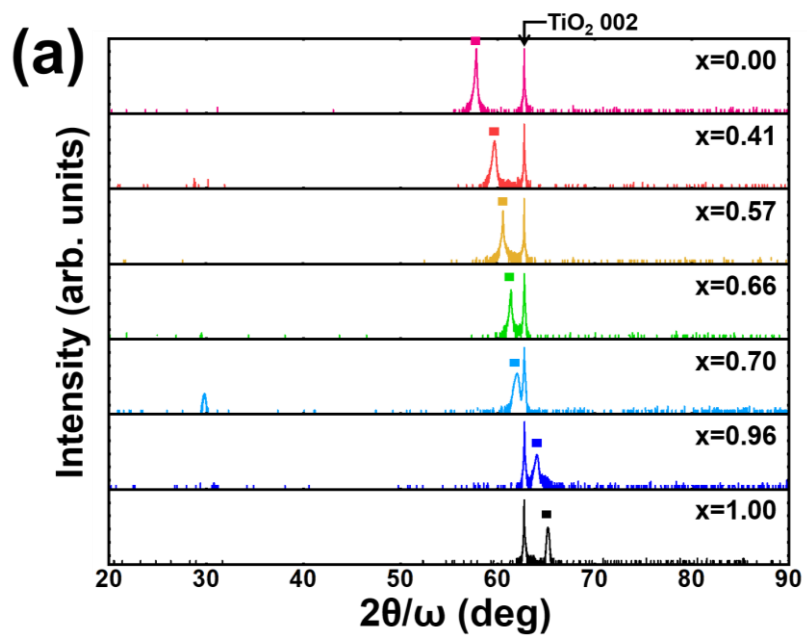
In order to evaluate crystalline quality of the alloy films, XRD symmetric rocking curve (RC) ω scan measurements were conducted. The RC- full width at half maximums (RC-FWHMs) of the 002 diffraction and thicknesses of the $r\text{-Ge}_x\text{Sn}_{1-x}\text{O}_2$ alloy films as a function of Ge compositions (x) are shown in Fig. 3. The film thicknesses were obtained by the SE analysis. The values of thickness of the films with $x=0.70$ and 1.00 were excluded because the SE analysis could not be applied for the two films as described below, although their thickness was estimated to be ~ 350 nm ($x=0.70$) from the growth rate of $x=0.66$, because these two compositions ($x=0.70$ and $x=0.66$) are almost the same as each other, and 500–1000 nm ($x=1.00$) due to the growth rate reported in Ref. 14. First of all, it should be noted that the RC-FWHMs of the end members of the alloys are ~ 100 arcsec ($x=0.00$) and ~ 500 arcsec ($x=1.00$), which are comparable to or slightly smaller than those of previously reported $r\text{-SnO}_2$ and $r\text{-GeO}_2$ films on TiO_2 (001) substrates.^{14,45} As shown in Fig. 3, the RC-FWHMs sharply increase for $x=0.70$ and 0.96, which means that crystallinities of $r\text{-Ge}_x\text{Sn}_{1-x}\text{O}_2$ degrade due to higher inclusion level of Ge as well as alloying compared to the end members, that is, SnO_2 and GeO_2 . In fact, Ge rich $r\text{-Ge}_x\text{Sn}_{1-x}\text{O}_2$ films ($x>0.5$) have not been demonstrated ever before, and $r\text{-GeO}_2$ was reported to show fluctuation in its

crystallinity^{14,15,46}, suggesting that Ge rich r-Ge_xSn_{1-x}O₂ and r-GeO₂ have poor stabilities. However, we believe that it is possible to improve the stability by preparing the compounds under optimized conditions. On the other hand, for $x=0.57$ and 0.66 , although the alloy films include relatively higher level of Ge, the RC-FWHMs are relatively small. As shown in Fig. 5 (a), which is described in detail later, the calculated lattice constant along the a -axis of r-Ge_xSn_{1-x}O₂ with Ge compositions of $0.5-0.6$ is found to be close to that of r-TiO₂ ($a_{\text{TiO}}=4.5941 \text{ \AA}$)²⁹. Therefore, for $x=0.57$ and 0.66 , it is considered that the decreased lattice mismatches around the mid-range of Ge composition lead to the small FWHMs of ~ 100 arcsec.

Then, we conducted the TEM observations for the r-Ge_xSn_{1-x}O₂ of $x=0.66$ and 0.96 . Figs. 4 (a) and (d) indicate cross-sectional TEM images at the r-Ge_{0.66}Sn_{0.34}O₂/r-TiO₂ and r-Ge_{0.96}Sn_{0.04}O₂/r-TiO₂ interface, respectively. Figs. 4 (b) and (e) show cross-sectional TEM images (bright-field) in two-beam diffraction condition with $\mathbf{g}=001$ and $\mathbf{g}=110$ at the r-Ge_{0.66}Sn_{0.34}O₂/r-TiO₂ and r-Ge_{0.96}Sn_{0.04}O₂/r-TiO₂ interface, respectively. Note that all the TEM images were viewed along the $\langle 110 \rangle$ zone axis. Selected area electron diffraction (SAED) patterns at the r-Ge_{0.66}Sn_{0.34}O₂/r-TiO₂ and r-Ge_{0.96}Sn_{0.04}O₂/r-TiO₂ interface are illustrated in Figs. 4 (c) and (f), respectively. Figs. 4 (a) and (b) suggest that there are few dislocations with components of Burgers vector $\mathbf{b}=\langle 001 \rangle$ and $\mathbf{b}=\langle 110 \rangle$ in the film with $x=0.66$. In the SAED pattern of $x=0.66$ in Fig. 4 (c), spots originating from the film are situated outside of and at almost the same positions as the r-TiO₂ spots along the $\langle 001 \rangle$ and $\langle 110 \rangle$ axes, respectively. Such positions of the spots are consistent with that the lattice mismatch along the a -axis decreases and the RC-FWHM is relatively low. Given the lattice mismatch along the a -axis described above, film thickness (208 nm) of the r-Ge_{0.66}Sn_{0.34}O₂ film on r-TiO₂, and almost the same positions of their SAED spots along the $\langle 110 \rangle$ axis, it is considered that the in-plane lattice relaxation did not occur or the relaxation ratio is small in the r-Ge_{0.66}Sn_{0.34}O₂/r-TiO₂. Therefore, less dislocation density in the film with $x=0.66$ may be attributed to such decreased lattice mismatch and resultant zero or small relaxation ratio. However, the critical thickness depends not only on lattice mismatches, but also on direction and size of Burgers vectors, slip plane of misfit dislocations, and so on. Thus, further studies and discussions are needed. On the other hand, as shown in Figs. 4 (d) and (e), there seems to be a large number of dislocations in the region near the interface in the film. The

dislocation density in the region near the interface is estimated to be over 10^{10} cm^{-2} based on the method of Ham.⁴⁷ The dislocations are considered to annihilate and/or coalesce above the region near the interface, and there seems to be much less dislocations in the region near the surface than the region near the interface. Furthermore, in Fig. 4(e), the two-beam diffraction condition observation with both $\mathbf{g}=001$ and $\mathbf{g}=110$ shows a lot of dislocations, indicating that both dislocations with screw component ($\mathbf{b}=\langle 001 \rangle$) and edge component ($\mathbf{b}=\langle 110 \rangle$) and/or mixed dislocations are present in the region near the interface in the r- $\text{Ge}_{0.96}\text{Sn}_{0.04}\text{O}_2$ film. In this study, although the r- GeO_2 film was not observed by the TEM, the RC-FWHM of the r- GeO_2 film in this work is compatible with the values reported in Refs. 14,46. Thus, it is considered that the r- GeO_2 film in this work possess the same amount of dislocations as reported in Refs. 14,46.

Here, the lattice constants of the r- $\text{Ge}_x\text{Sn}_{1-x}\text{O}_2$ alloy films were obtained by the XRD and TEM. Those along the a - and c -axis were obtained from 220 diffraction peaks of in-plane $2\theta/\Phi$ scans and 002 diffraction peaks of the symmetric $2\theta/\omega$ scans, respectively. Note that a -axis length of $x=0.57$ and 0.66 cannot be acquired by the $2\theta/\Phi$ scans because their values are relatively similar to that of r- TiO_2 , and it is difficult to identify the 220 diffraction peaks originated from the films. For $x=0.66$ and 0.96 , the lattice constants were also estimated from the SAED pattern shown in Figs. 4 (c) and (f). We corrected the experimental values based on the lattice parameters of r- TiO_2 ($a_{\text{TiO}}=4.5941 \text{ \AA}$ and $c_{\text{TiO}}=2.9589 \text{ \AA}$)²⁹ in the calculations. Figs. 5 (a) and (b) depict the experimentally obtained and calculated lattice constants along the a - and c -axis, respectively, as a function of Ge compositions (x), as well as the those previously reported for the end members.²⁹ It is confirmed that the lattice constants both along the a - and c -axis decrease as Ge compositions (x) increase. Besides, as presented in both Figs. 5 (a) and (b), this trend of the experimental values is well consistent with not only those derived by the DFT calculations, but also those expected by the Vegard's law based on the referred values (green dashed lines).



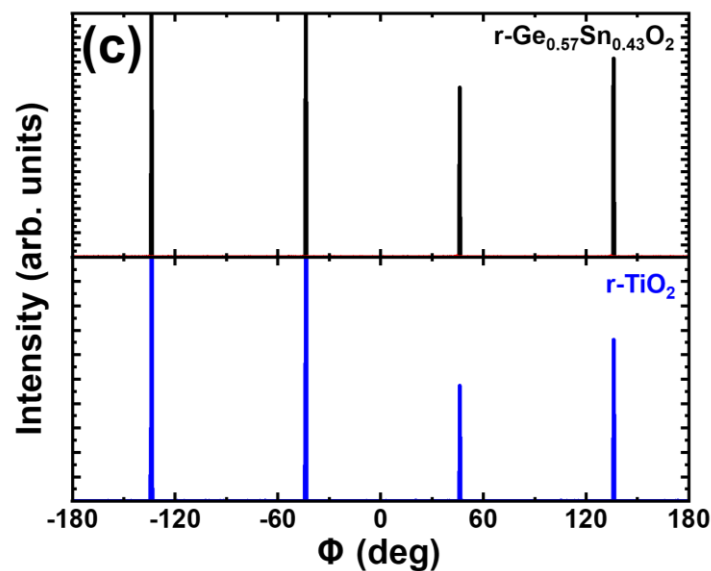


Fig. 2 XRD symmetric $2\theta/\omega$ scan profiles of $r\text{-Ge}_x\text{Sn}_{1-x}\text{O}_2$ alloy thin films on $r\text{-TiO}_2$ (001) substrates in a wide (a) and a narrow range (b). The compositions of Ge (x) in the thin films were determined by the EDS. The solid squares in (a) represent 002 diffraction peaks of $r\text{-Ge}_x\text{Sn}_{1-x}\text{O}_2$ alloy thin films. (c) XRD (301) Φ scan profile of $r\text{-Ge}_{0.57}\text{Sn}_{0.43}\text{O}_2$ alloy thin films (Black line) and $r\text{-TiO}_2$ substrate (Blue line).

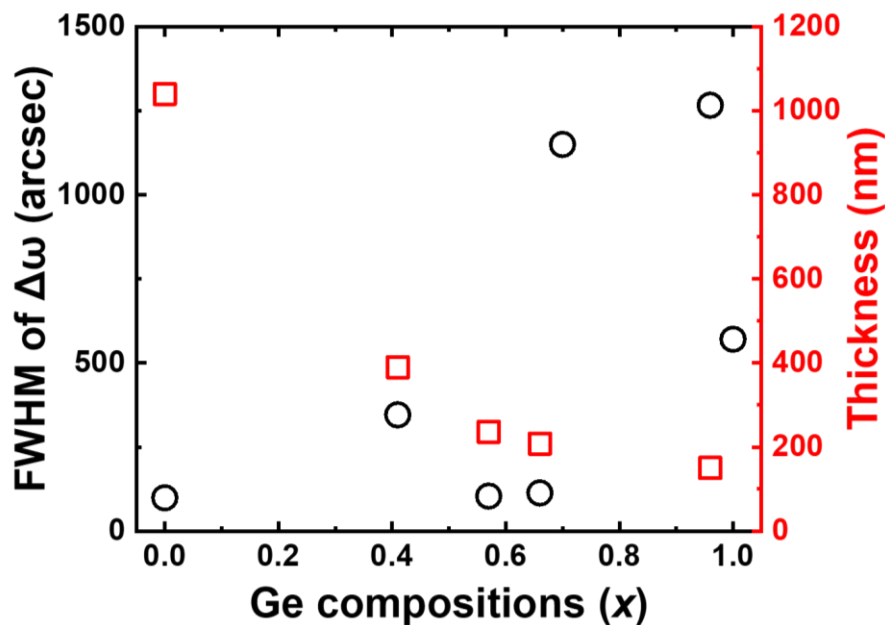
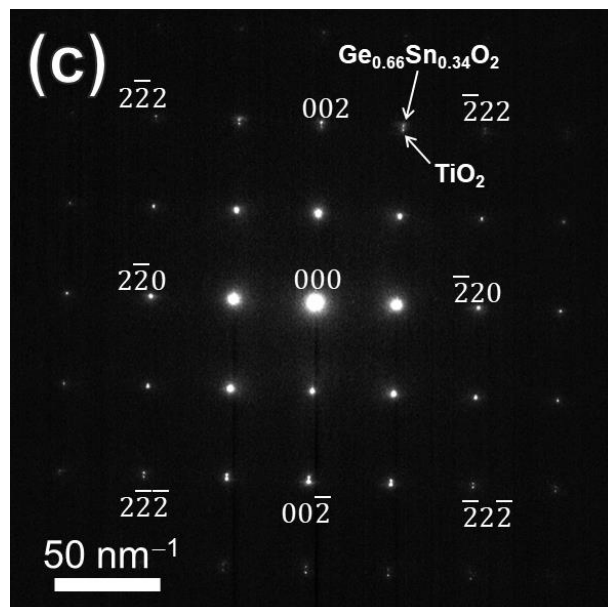
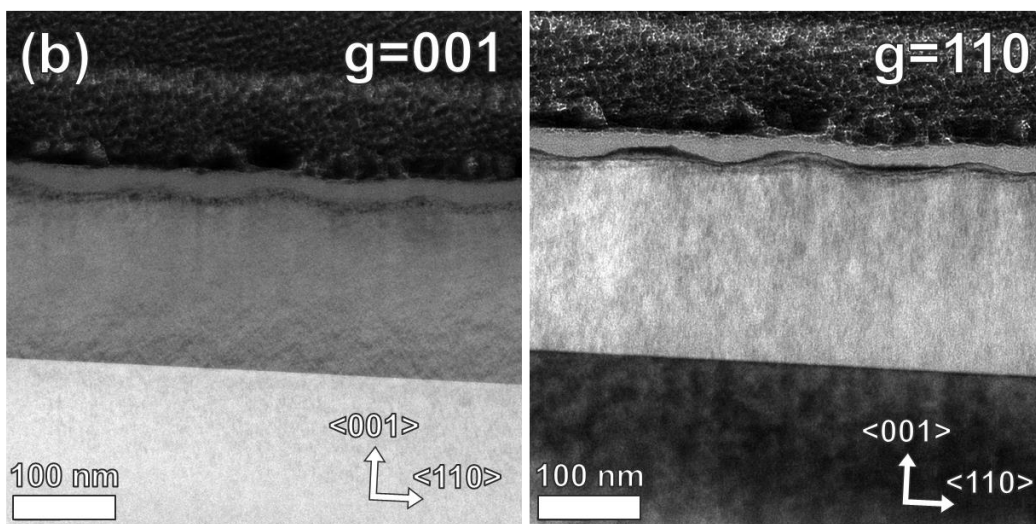
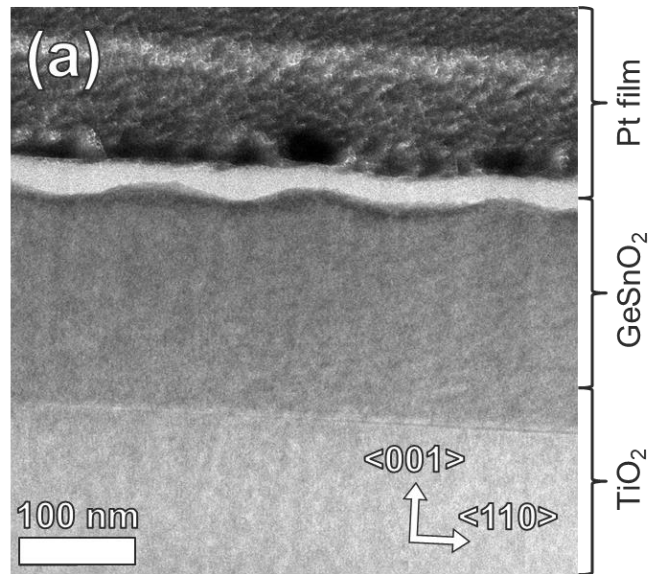


Fig. 3 XRD symmetric RC-FWHMs (Black balls) and thicknesses obtained by the SE (Red squares) of $r\text{-Ge}_x\text{Sn}_{1-x}\text{O}_2$ alloy films as a function of Ge compositions (x). The thicknesses films with $x=0.70$ and 1.00 are excluded.



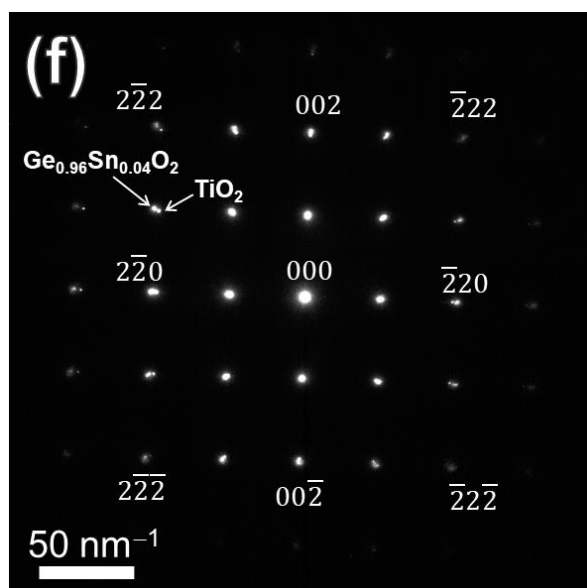
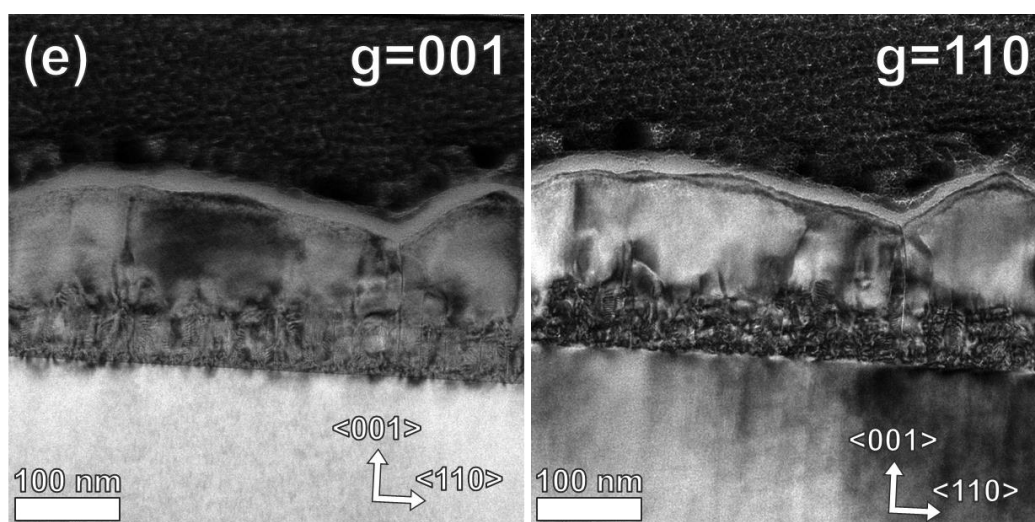
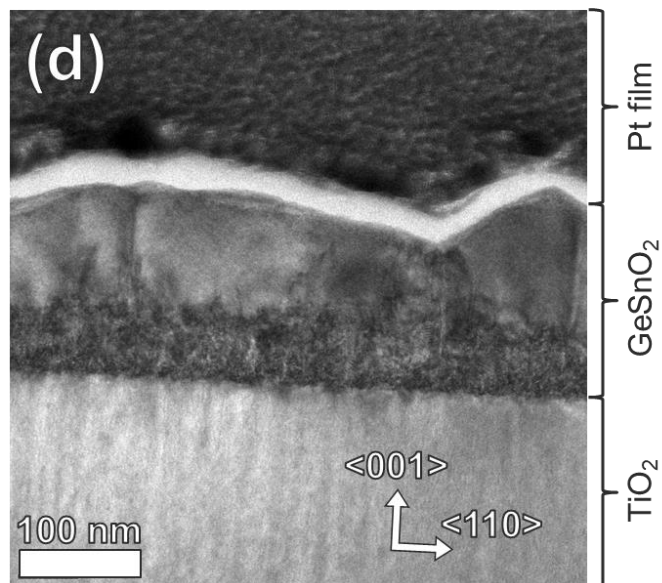


Fig. 4 Cross-sectional TEM images at (a) $r\text{-Ge}_{0.66}\text{Sn}_{0.34}\text{O}_2/r\text{-TiO}_2$ and (d) $r\text{-Ge}_{0.96}\text{Sn}_{0.04}\text{O}_2/r\text{-TiO}_2$ interface. Cross-sectional TEM images (bright-field) in two-beam diffraction condition with $\mathbf{g}=001$ and $\mathbf{g}=110$ at (b) $r\text{-Ge}_{0.66}\text{Sn}_{0.34}\text{O}_2/r\text{-TiO}_2$ and (e) $r\text{-Ge}_{0.96}\text{Sn}_{0.04}\text{O}_2/r\text{-TiO}_2$ interface. SAED patterns at (c) $r\text{-Ge}_{0.66}\text{Sn}_{0.34}\text{O}_2/r\text{-TiO}_2$ and (f) $r\text{-Ge}_{0.96}\text{Sn}_{0.04}\text{O}_2/r\text{-TiO}_2$ interface. All the TEM images were viewed along the $\langle 110 \rangle$ zone axis.

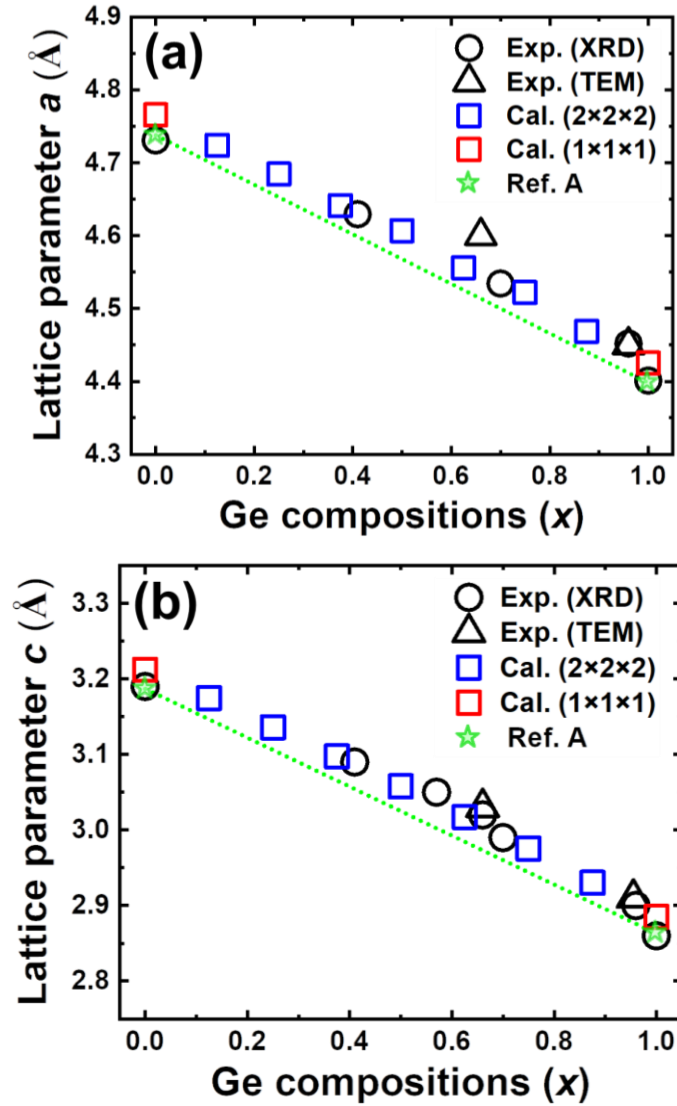


Fig. 5 Experimentally obtained and calculated lattice constants of $r\text{-Ge}_x\text{Sn}_{1-x}\text{O}_2$ alloy thin films along (a) the a - and (b) c -axis as a function of Ge compositions (x). Black circle and triangles, Blue and red squares represent experimental values obtained by XRD and TEM, calculated values with supercell of $2 \times 2 \times 2$ and $1 \times 1 \times 1$, respectively. Green stars and dashed lines represent values of lattice parameters cited from Ref. A (Ref. 29) and those expected by the Vegard's law based on the referred values.

B. Surface, chemical, and crystalline characterization by SEM, EDS, and EBSD

Fig. 6 (a) illustrates plane-view SEM images of $r\text{-Ge}_x\text{Sn}_{1-x}\text{O}_2$ films with $x=0.00, 0.41, 0.57, 0.66, 0.70, 0.96,$ and 1.00 . As shown in Fig. 6 (a), there seems to be some pits or somethings on the surface of the films with $x=0.57$ and 0.66 , and the surface of the film with $x=0.70$ seems rough. Additionally, for $x=1.00$, phase separation can be seen, that is, one surface area is rough, and the other is smooth.

Fig. 6 (b) exhibits plane-view EDS mappings of $r\text{-Ge}_x\text{Sn}_{1-x}\text{O}_2$ films with $x=0.57$ and 1.00 . The observed areas are the same as the SEM images in Fig. 6 (a). For $x=0.57$, it is confirmed that Ge, Sn, and O are uniformly distributed and there is no remarkable phase separation area in the film. It should be noted that no other elements were detected except for Ti, which is a component of the substrates used in this work and Ti was detected because the penetration depth of the incidence electrons was longer than the film thickness and the incidence electrons reach the substrate. This uniform distribution of elements and no phase separation were also observed for the films with $x=0.00, 0.41, 0.66, 0.70,$ and 0.96 . On the other hand, for $x=1.00$, the color strength of Ge is uniform in each area (the rough surface area and the smooth surface area), but different from each other. This is because the $r\text{-Ge}_x\text{Sn}_{1-x}\text{O}_2$ with $x=1.00$ shows fluctuation in its thickness as reported in Ref. 46, and the integral intensity for Ge becomes brighter in the thicker area. No other elements except for Ge, O, and Ti were detected for $x=1.00$.

In order to analyze the crystallographic orientation of $r\text{-Ge}_x\text{Sn}_{1-x}\text{O}_2$ films and phase separation in the $r\text{-Ge}_x\text{Sn}_{1-x}\text{O}_2$ with $x=1.00$, the EBSD measurements were conducted. In the measurements, the coordinates of the equipment were set as follows; the z -axis of the equipment is parallel to the $\langle 001 \rangle$ axis of TiO_2 substrate and the x - and y -axes of the equipment are parallel to the equivalent $\langle 110 \rangle$ axes of TiO_2 substrate. In this work, in order to analyze the measured EBSD patterns and detect crystallographic orientations of the films, we used crystallographic data including chemical compositions, space group, cell parameters, and atom coordinates of $r\text{-SnO}_2$ and $r\text{-GeO}_2$ ²⁹ for the films with $x=0.00$ and 1.00 , respectively. For the analysis of the EBSD patterns of the films with $x=0.41, 0.57, 0.66, 0.70,$ and 0.96 , we prepared original data, where chemical compositions are set to x values, space group and atom coordinates are the same as conventional rutile structure, and cell parameters are estimated by using the Vegard's law. Fig. 6 (c) exhibits the EBSD inverse pole figure (IPF)

maps along the x -, y -, and z -axes. The observed areas are shown by the SEM images in the left hand. The color map indicating plane orientations is also illustrated in the bottom right. For $x=0.57$, the EBSD IPF map along the z -axis and those along the x - and y -axis correspond well to (001) and (110) orientations, respectively, of the rutile structure, indicating that both the out-of-plane and in-plane orientations of the $r\text{-Ge}_x\text{Sn}_{1-x}\text{O}_2$ with $x=0.57$ and $r\text{-TiO}_2$ substrate are consistent with each other, and the film are epitaxially grown on the substrate. The same results were obtained for $x=0.00, 0.41, 0.66, 0.70,$ and 0.96 . On the contrary, for $x=1.00$, although the same results are observed and the same out-of-plane and in-plane orientations between the film and substrate were confirmed in rough surface area, the EBSD IPF map along all the axis shows almost no orientation of the rutile structure in the smooth surface area. This result suggests that the $r\text{-Ge}_x\text{Sn}_{1-x}\text{O}_2$ with $x=1.00$ shows fluctuation in its crystallinity as reported in Ref. 46 as well as in its thickness. The black points in the well-crystallized region are attributed to multiple scattering of diffraction electrons by its rough surface.

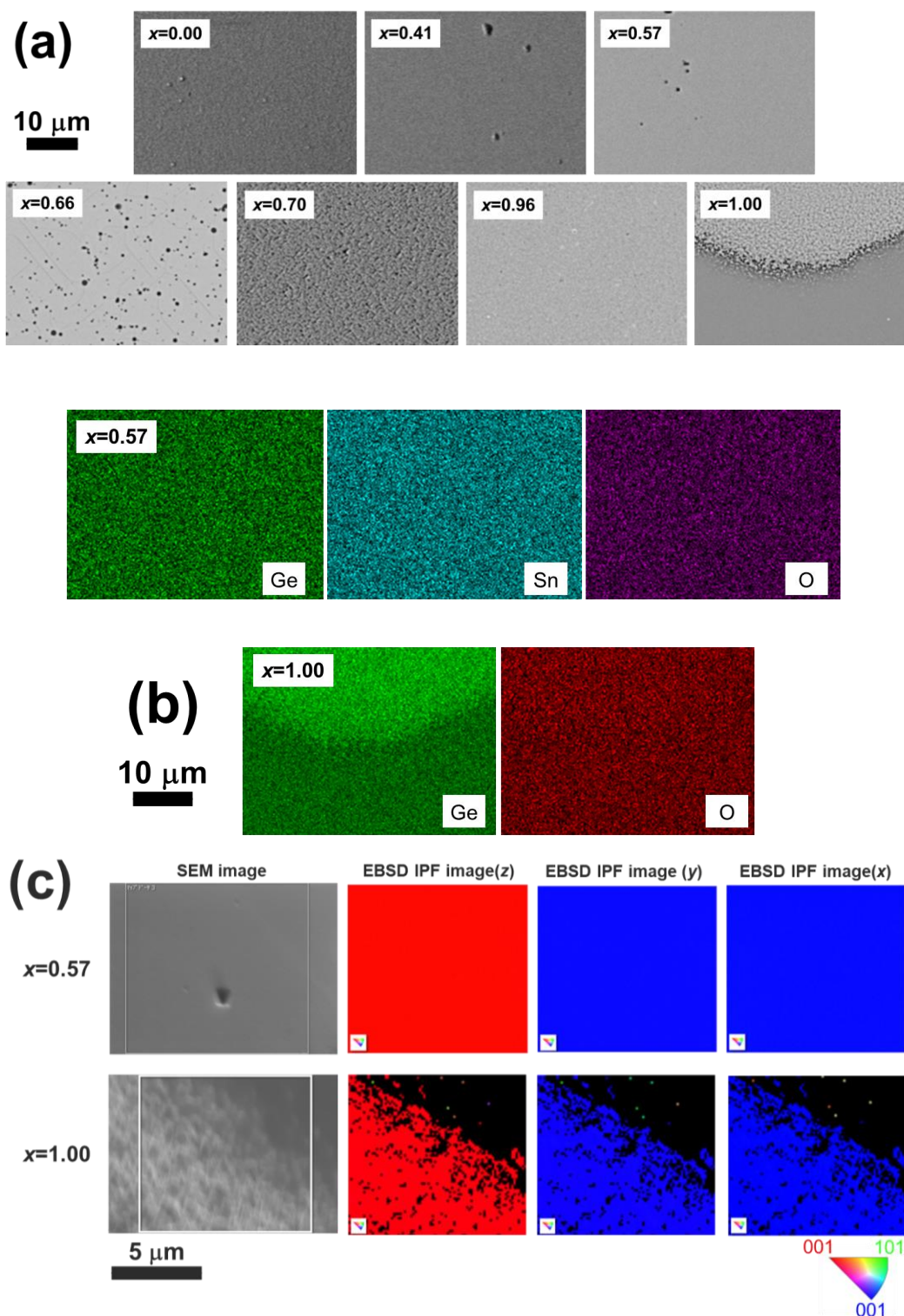


Fig. 6 (a) Plane-view SEM images of $r\text{-Ge}_x\text{Sn}_{1-x}\text{O}_2$ films with $x=0.00, 0.41, 0.57, 0.66, 0.70, 0.96$ and 1.00 . (b) Plane-view EDS mapping of $r\text{-Ge}_x\text{Sn}_{1-x}\text{O}_2$ films with $x=0.57$ and 1.00 . The observed areas are consistent with the SEM images in Fig. 6 (a). (c) Plane-view EBSD mapping of $r\text{-Ge}_x\text{Sn}_{1-x}\text{O}_2$ films with $x=0.57$ and 1.00 . The observed areas are shown by white squares in the SEM (Left).

C. Modulation of bandgaps and electronic structures

In order to estimate bandgaps of the r-Ge_xSn_{1-x}O₂ alloy thin films, we performed SE analysis for the films with $x=0.00, 0.41, 0.57, 0.66,$ and 0.96 . In the analysis, we used Tauc-Lorenz (T-L) dispersion formula^{48,49} as a fitting model for ellipsometric parameters (Δ, Ψ), which are related to the complex ratio of the Fresnel reflection coefficients as $\rho=\tan\Psi\exp(i\Delta)$. For $x=0.70, 1.00$, measured ellipsometric parameters cannot be well fitted by the T-L model due to the rough surface ($x=0.70, 1.00$). Besides, for $x=1.00$, the ill-fitting is also affected by the fluctuation in its thickness and crystallinity in plane as described above and in Ref. 46.

In this study, the bandgaps were determined using Tauc plot. Nagasawa and Shinomiya reported that the bandgap of rutile-structured SnO₂ was direct-forbidden^{50,51}, and the bandgaps have been acquired assuming the direct-forbidden transitions for r-SnO₂ and r-GeO₂^{4,21}. Thus, we also assumed the direct-forbidden transition for the r-GeSnO₂ alloys in this work. Assuming direct-forbidden transition, the absorption coefficient (α) and the bandgap (E_g) are described as follows^{52,53},

$$(\alpha h\nu)^{1/n} = A(h\nu - E_g), \quad n = 3/2, \quad (1)$$

where $h\nu$ is incidence photon energy and A is a constant. The absorption coefficient is represented by $\alpha=4\pi k/\lambda$ using the derived extinction coefficient k and the incidence wavelength λ . Fig. 7 (a) shows the relationships between $(\alpha h\nu)^{2/3}$ and the incidence photon energy. The bandgaps were estimated from the intersection of the extrapolated straight line, which is the liner fitting of the $(\alpha h\nu)^{2/3}-h\nu$ plots, with the photon energy axis, and found to be 3.81 ($x=0.00$), 3.95 ($x=0.41$), 3.98 ($x=0.57$), 4.02 ($x=0.66$), and 4.44 eV ($x=0.96$). The obtained bandgaps of r-Ge_xSn_{1-x}O₂ ($x\leq 0.96$) as a function of the Ge compositions (x) are shown in Fig. 7 (b). For $x=1.00$, we adopted the value of bulk r-GeO₂ reported in Ref. 4 (blue triangle) because we could not estimate its bandgap from the SE analysis for the present thin film. It is confirmed that the bandgap value of r-Ge_xSn_{1-x}O₂ increases as Ge composition increases in a Ge composition range of $0.00\leq x\leq 0.96$. In addition, like typical alloy semiconductors, there seems to be the bandgap bowing in r-Ge_xSn_{1-x}O₂ alloys. Using a bowing parameter (b), which is a degree of deviations of alloy's bandgap values from the linear interpolation of the values of endpoint constituents, bandgaps of r-Ge_xSn_{1-x}O₂ ($E_g^{\text{GeSnO}}(x)$) can be expressed as

$$E_g^{\text{GeSnO}}(x) = xE_g^{\text{GeO}} + (1-x)E_g^{\text{SnO}} - bx(1-x), \quad (2)$$

where E_g^{GeO} and E_g^{SnO} are the bandgaps of r-GeO₂ and r-SnO₂, which were set at 4.68 eV⁴ and 3.81 eV, respectively. By curve fitting shown in Fig. 5 (b), the bowing parameter of the alloy system was estimated to be 1.2 eV.

In order to deeply analyze the shift of bandgaps and electronic structures in r-Ge_xSn_{1-x}O₂ alloys accompanying the Ge compositions change, we used the first-principles calculations. First, we compared the experimental and calculated bandgap values. It is a common phenomenon that the first-principle calculations underestimate bandgap values unless using frameworks with high cost such as hybrid functionals⁵⁴⁻⁵⁶, GW approximation^{57,58}, which originates from the lack of derivative discontinuity and spurious self-interaction. However, it is unrealistic to use such accurate but high-cost methods of calculations for alloys treated in the present study, because a large cell is needed to accurately calculate the electronic structure of alloys containing different types of elements with a wide range of compositions. Therefore, we used the TB-mBJ (Meta-GGA) method which relatively balance the cost and accuracy as described above. Calculations with a heavy cost gave values (PBE0: 3.8 eV⁷, G₀W₀@HSE06: 3.89 eV⁵⁹) for SnO₂ which is well consistent with our experimentally obtained value (3.81 eV). To correct the underestimation of calculated bandgap values, we compared experimental and calculated ΔE_g . Here, we define each ΔE_g as $\Delta E_g = E_g - E_g^{\text{SnO}}$, where E_g and E_g^{SnO} are the bandgap values of r-Ge_xSn_{1-x}O₂ alloys and r-SnO₂, respectively. The experimental and calculated E_g^{SnO} are 3.81 and 3.48 eV, respectively. Fig. 8 (a) presents experimental and calculated ΔE_g as a function of Ge compositions (x). From Fig. 8 (a), it can be said that the bandgap modulation with Ge compositions experimentally obtained is supported by the calculations.

Then, we present a calculated natural band alignment of r-Ge_xSn_{1-x}O₂ alloys as a function of Ge compositions (x) in Fig. 8 (b). The energy values are referenced to the vacuum level. In Fig. 8 (b), it is estimated that both the conduction band minimum (CBM) and valence band maximum (VBM) become shallow as Ge compositions (x) increase. The heterojunction of r-Ge_xSn_{1-x}O₂ with different compositions was found to be a staggered-gap (type-II) in an almost entire range of Ge compositions (x). The trend of the VBM in r-Ge_xSn_{1-x}O₂ alloys with an increase in Ge compositions (x) agrees with the shallowing of the VBM from r-SnO₂ to r-GeO₂ reported in Refs. 5,7, though the VBM offset of r-SnO₂/r-

GeO₂ is relatively smaller than those in Refs. 5,7 due to our calculation with lower cost. This trend in shallowing of the VBM is considered to be a key for achievement of p-type doping in r-GeO₂ (and highly Ge-rich r-Ge_xSn_{1-x}O₂ alloys) as mentioned just below. The Fermi level lies within the n-type and p-type Fermi pinning energies ($E_{\text{pin}}^{\text{n}}$ and $E_{\text{pin}}^{\text{p}}$, respectively), which are roughly universal for materials with a similar chemical group, such as III-V, II-VI materials, and metal oxides.⁶⁰⁻⁶⁴ (For oxide semiconductors, $E_{\text{pin}}^{\text{n}}$ and $E_{\text{pin}}^{\text{p}}$ lie at about 3.5 and 6.5 eV below the vacuum level, respectively⁶⁴) In other words, if the Fermi level rises above $E_{\text{pin}}^{\text{n}}$ or drops below $E_{\text{pin}}^{\text{p}}$, compensation defects will spontaneously form, pinning the Fermi level at $E_{\text{pin}}^{\text{n}}$ and $E_{\text{pin}}^{\text{p}}$. As a consequence, the shallower the VBM becomes, the higher the efficiency of p-type doping would be. Furthermore, intrinsic properties of given materials for doping efficiencies have also been similarly discussed in terms of the amphoteric defect model and Fermi-level stabilization energy.⁶⁵⁻⁶⁸ Thus, our result, which indicates the trend in shallowing of the VBM with an increase in Ge compositions, encourages realization of p-type doping in r-GeO₂ (and highly Ge-rich r-Ge_xSn_{1-x}O₂ alloys) and should contribute to further discussions and challenges for fabrication of new p-type oxide semiconductors, though the calculated VBM of r-GeO₂ seems deeper than the $E_{\text{pin}}^{\text{p}}$ (6.5 eV below the vacuum level) due to our calculation with lower cost.

In the end of the section, the natural band alignment of r-Ge_xSi_{1-x}O₂ alloys is shown in Fig. 8 (c). It is confirmed that as Si compositions increase, the bandgap of r-Ge_xSi_{1-x}O₂ alloys sharply increase (4.28–7.70 eV). At the same time, the CBM becomes shallower and the VBM become deeper with an increase in Si compositions, indicating that the interface of r-Ge_xSi_{1-x}O₂ with different alloy compositions is type-I. In addition, as found in Fig. 8 (c), r-SiO₂ and Si-rich r-Ge_xSi_{1-x}O₂ alloys have shallow CBM and deep VBM, suggesting that it may be extremely difficult to achieve both n-type and p-type conduction from a viewpoint of the Fermi pinning energy and/or the Fermi-level stabilization energy as mentioned above. However, these large CBM and VBM offset is considered to be preferable to use them as a blocking layer of other rutile-structured devices.

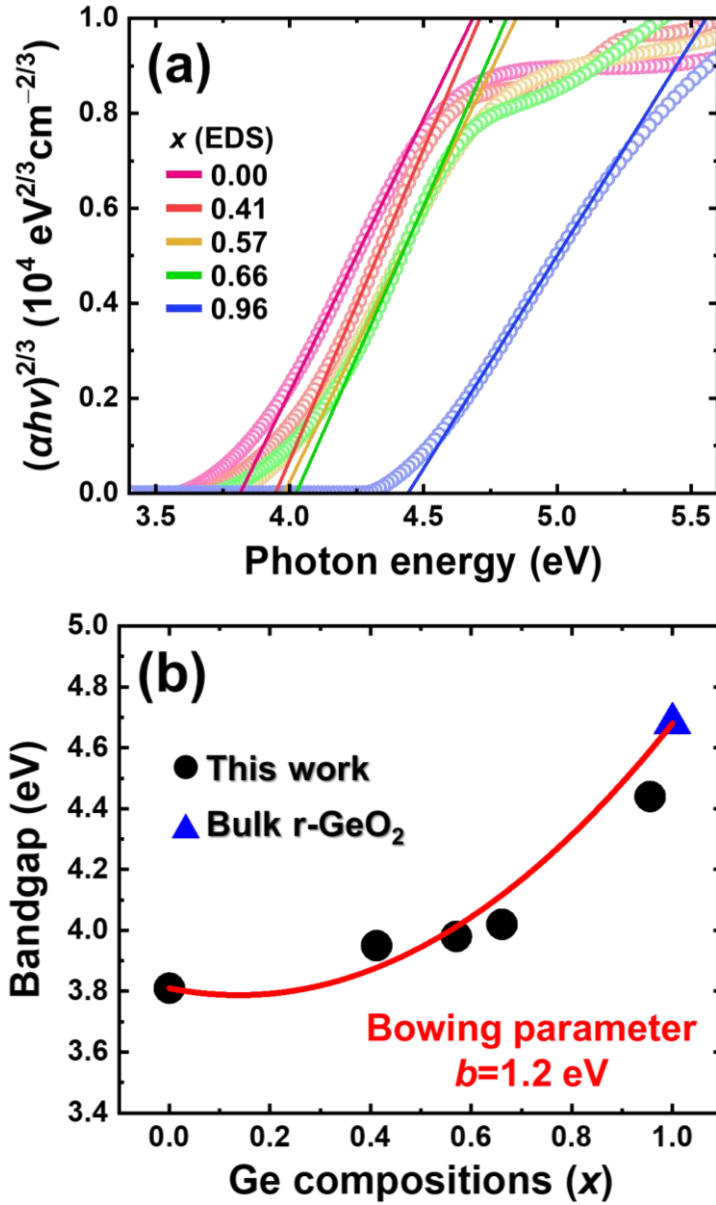
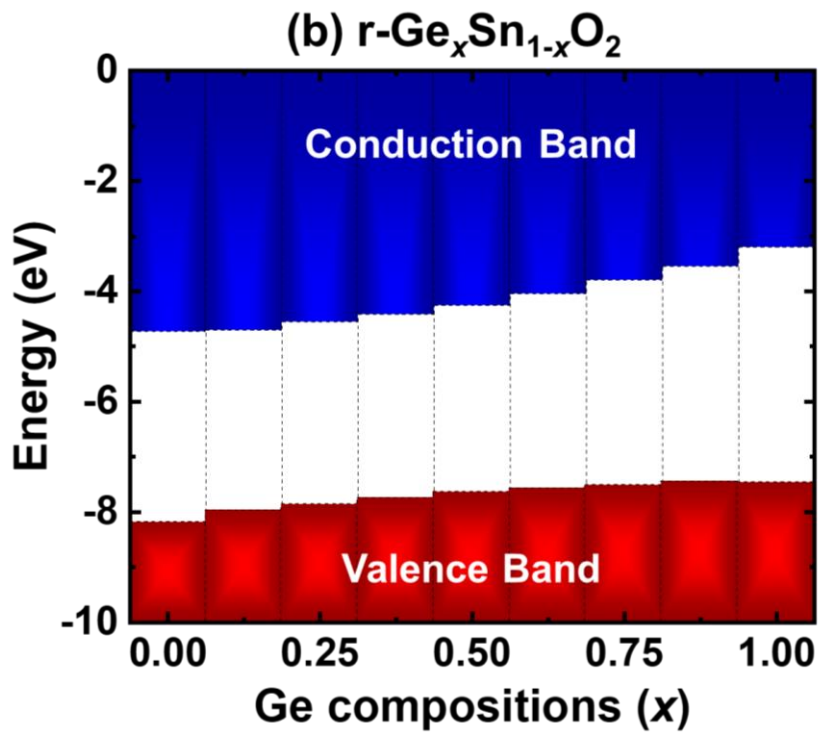
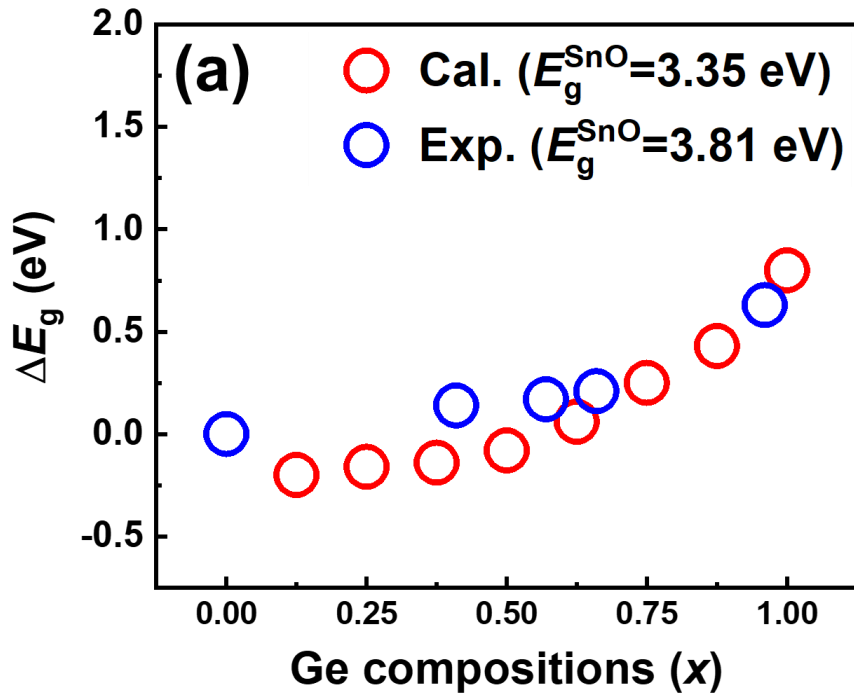


Fig. 7 (a) Relationships between $(\alpha h\nu)^{2/3}$ and the incidence photon energy in $r\text{-Ge}_x\text{Sn}_{1-x}\text{O}_2$ alloy thin films with $x=0.00, 0.41, 0.57, 0.66,$ and 0.96 (Blank circles). The solid lines represent the linear fitting of the $(\alpha h\nu)^{2/3}$ - $h\nu$ plots. The bandgaps were estimated from the intersection with the photon energy axes. (b) The bandgaps of $r\text{-Ge}_x\text{Sn}_{1-x}\text{O}_2$ alloy thin films obtained by the SE measurements and the Tauc plots for the direct-forbidden transitions as a function of Ge compositions (Black balls) and that of bulk $r\text{-GeO}_2$ (Blue triangle)⁴. The bowing parameter b was found to be 1.2 eV by curve fitting (Red line).



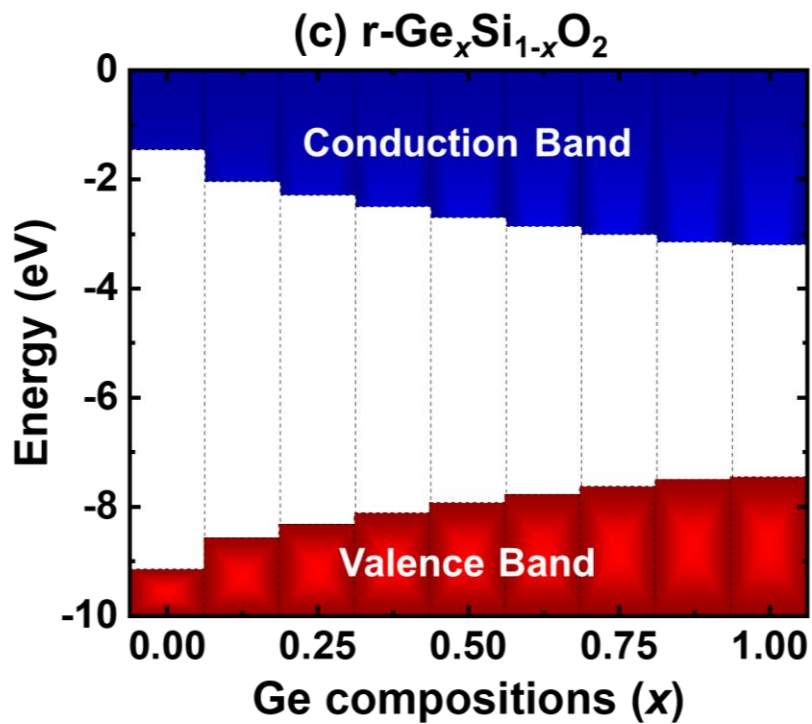


Fig. 8 (a) Experimental (Blue circle) and calculated (Red circle) ΔE_g as a function of Ge compositions (x). The bandgap values for r-SnO₂ (E_g^{SnO}) of 3.81 eV and 3.35 eV, respectively, and each ΔE_g are defined as $\Delta E_g = E_g - E_g^{\text{SnO}}$, where E_g is bandgaps of r-Ge_xSn_{1-x}O₂ alloy films. (b) Calculated natural band alignment of r-Ge_xSn_{1-x}O₂ alloys as a function of Ge compositions. (c) Calculated natural band alignment of r-Ge_xSi_{1-x}O₂ alloys as a function of Ge compositions. The energy values are referenced to the vacuum level in both (b) and (c).

C. Electrical properties

We investigated electrical properties of the $r\text{-Ge}_x\text{Sn}_{1-x}\text{O}_2$ alloy films ($x=0.00, 0.41, 0.57, 0.66, 0.70$ and 0.96) by the four-probe method and Hall effect measurements with the van der Pauw configuration. As described in the experimental section, all the samples in this work were grown without intentional doping. We excluded the sample with $x=1.00$ because it is difficult to measure the accurate property of crystallized $r\text{-GeO}_2$ due to fluctuation in its crystallinity. Fig. 9 (a) shows the resistivities of $r\text{-Ge}_x\text{Sn}_{1-x}\text{O}_2$ measured by the four-probe method as a function of Ge compositions (x), indicating that the $r\text{-Ge}_x\text{Sn}_{1-x}\text{O}_2$ of $x\leq 0.96$ shows relatively high conductivity without intentional doping. Figs. 9 (b) and (c) exhibit the carrier concentrations and mobilities of $r\text{-Ge}_x\text{Sn}_{1-x}\text{O}_2$ films determined by the Hall effect measurements as a function of Ge compositions (x). The Hall effect measurements with DC magnetic field demonstrate that $r\text{-Ge}_x\text{Sn}_{1-x}\text{O}_2$ with $x\leq 0.57$ manifests n-type conductivity. In order to further confirm the carrier type and whether a single carrier model applies, we also measured the Hall voltages under varied magnetic fields for the $r\text{-Ge}_x\text{Sn}_{1-x}\text{O}_2$ with $x=0.00, 0.41, \text{ and } 0.57$. As shown in Fig. 9 (d), the Hall voltages are negatively proportional to the applied magnetic fields for $r\text{-Ge}_{0.57}\text{Sn}_{0.43}\text{O}_2$, which confirms n-type conductivity and availability of a single-carrier model. The negative linear dependences of the Hall voltages on the applied magnetic fields were also observed for the films with $x=0.00, 0.41$.

Hydrogen-related defects including interstitial hydrogen (H_i), hydrogen on an oxygen site (H_O) are considered to be one of dominant carrier (electron) sources because it is theoretically reported that both H_i^+ and H_O^+ have low formation energy and act as shallow donors in both $r\text{-SnO}_2$ ^{69,70} and $r\text{-GeO}_2$ ⁵. In addition, muon spin resonance (μSR) spectroscopy suggests that hydrogen forms a shallow-donor center in SnO_2 .⁷¹ Hydrogen can be supplied by H_2O , which is carried to the reaction area as the source solution in the mist CVD method. As indicated in Figs. 9 (b), the carrier concentrations increase as Ge compositions increase, suggesting that the hydrogen-related defects may increase by incorporating Ge in $r\text{-SnO}_2$. In addition, Fig. 9 (c) shows that the mobilities decrease as Ge compositions increase, which is probably because the alloy scattering, due to a disorder potential arising from the random distribution of the constituent atoms among the available lattice sites, is remarkable in the mid-range of alloy composition⁷²⁻⁷⁴. Moreover, inclusion of pits for $x=0.57$, as found in Fig. 6 (a), restrict carrier mobility. On the other hand, it should

be noted that oxygen vacancy (V_O) is theoretically reported to act as a deep donor in both r-SnO₂⁷⁰ and r-GeO₂⁵, thus, V_O may not be a main carrier source, which is in contradiction with the conventional attribution of n-type conductivity in SnO₂ to V_O . However, at this moment it is difficult to determine exact origin of a main carrier source in the present thin films. Thus, further studies are needed to specify it. For $x=0.66$, 0.70 and 0.96, the carrier type, carrier concentration, and mobility cannot be identified by the Hall effect measurements owing to scattered data, probably because carrier mobility is so low the Hall voltages are not accurately obtained. This is probably because the alloy scattering is significantly effective, the film with $x=0.66$ include some pits, and/or the crystallinity of the films with $x=0.70$ and 0.96 is drastically degraded as mentioned above. Nevertheless, it should be noted that the films with $x \leq 0.57$ exhibit n-type conductivity and those with $x=0.66$, 0.70, and 0.96 manifest resistivities lower than 1 Ωcm , though the electrical properties become inferior with increase Ge compositions.

Finally, in this study, we only prepared undoped r-Ge_xSn_{1-x}O₂ alloy films, therefore, relationships between doping and electrical properties in the alloy should be investigated in the future. From this point of view, several experimental and theoretical reports on binary r-SnO₂ and r-GeO₂ suggest that F^{5,75}, Sb^{5,76}, As⁵, Ta⁴⁵, and Al⁵, Ga⁹, In⁵ are considered to be candidates for n-type and p-type dopants, respectively. Chae et al., proposed that co-doping acceptors with hydrogen and subsequent annealing like GaN with Mg was one of strategies for achieving p-type doping⁵. Thus, both experimental and theoretical studies are also needed.

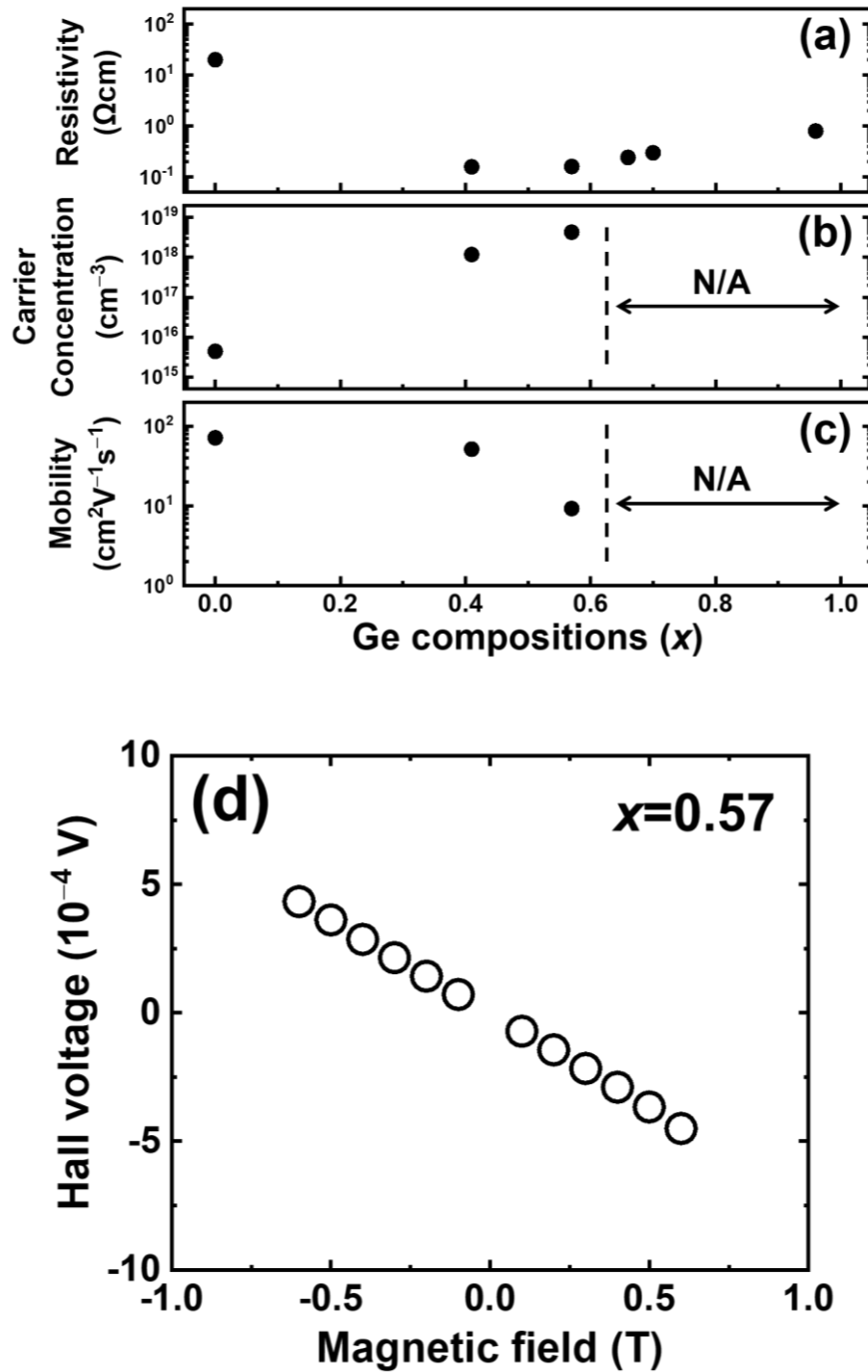


Fig. 9 (a) Resistivities, (b) carrier concentrations, and (c) mobilities of $r\text{-Ge}_x\text{Sn}_{1-x}\text{O}_2$ alloy thin films as a function of Ge compositions (x). (d) Relationship between the Hall voltages and applied magnetic fields of $r\text{-Ge}_{0.57}\text{Sn}_{0.43}\text{O}_2$ alloy thin film.

4. Conclusion

In this study, we proposed an ultra-wide bandgap alloy system based on rutile-structured oxides ($\text{GeO}_2\text{-SnO}_2\text{-SiO}_2$) and reported results of experimental investigations and the first-principles calculations. Experimentally, we fabricated (001)-oriented $\text{r-Ge}_x\text{Sn}_{1-x}\text{O}_2$ alloy thin films on r-TiO_2 (001) substrates with an entire range of Ge compositions (x) by the mist CVD technique. From the structural characterizations including the XRD, EDS and EBSD, it is clear that the fabricated $\text{r-Ge}_x\text{Sn}_{1-x}\text{O}_2$ alloy films with $x \leq 0.96$ and the well-crystallized area in the film with $x=1.00$ have uniform distribution of Ge, Sn, and O, and the rutile-structure with the same in-plane and out-of-plane orientation as r-TiO_2 substrates. The TEM observations display few dislocations in $\text{r-Ge}_{0.66}\text{Sn}_{0.34}\text{O}_2$ probably because the in-plane lattice mismatch is relatively small. On the other hand, there are a lot of both edge and screw or mixed dislocations near the film/substrate interface in $\text{r-Ge}_{0.96}\text{Sn}_{0.04}\text{O}_2$. The lattice constants both along the a - and c -axis decrease with an increase in Ge compositions. The values of lattice constants and their compositional dependence are in good agreement with those obtained by our calculations. The SE analysis demonstrates that their bandgaps increase as Ge compositions increase (3.81–4.44 eV), with a bowing parameter of 1.2 eV. The trend of experimentally determined bandgaps of the $\text{r-Ge}_x\text{Sn}_{1-x}\text{O}_2$ alloy films are generally consistent with that of the calculations. Moreover, we presented the calculated natural band alignments of $\text{r-Ge}_x\text{Sn}_{1-x}\text{O}_2$ and $\text{r-Ge}_x\text{Si}_{1-x}\text{O}_2$ alloys. The results indicate that the shallowing of the VBM in $\text{r-Ge}_x\text{Sn}_{1-x}\text{O}_2$ takes place as the increase in Ge compositions, which is considered to be a key for achieving p-type conduction in r-GeO_2 and Ge-rich $\text{r-Ge}_x\text{Sn}_{1-x}\text{O}_2$. It was also found that the bandgaps of $\text{r-Ge}_x\text{Si}_{1-x}\text{O}_2$ alloys sharply increase with the CBM shallowing and the VBM deepening as Si compositions increase, suggesting that it is preferable to use r-SiO_2 and Si-rich $\text{r-Ge}_x\text{Si}_{1-x}\text{O}_2$ as a blocking layer of other rutile-structured devices. Our measurements of electrical properties indicate that the $\text{r-Ge}_x\text{Sn}_{1-x}\text{O}_2$ ($x \leq 0.57$) exhibit n-type conductivities. For the $\text{r-Ge}_x\text{Sn}_{1-x}\text{O}_2$ ($x \leq 0.57$), as Ge compositions increase, the carrier concentrations and mobilities become higher and lower, respectively. In addition, even the $\text{r-Ge}_x\text{Sn}_{1-x}\text{O}_2$ with $x=0.66$, 0.70 and 0.96 show resistivities lower than 1 Ωcm .

We believe that our experimental and theoretical results give rise to fruitful

information for further researches and developments of the alloy system based on rutile-structured oxides as well as r-GeO₂, r-SnO₂, and r-SiO₂ for power-device applications.

Acknowledgments

This work was supported, in part, by JSPS KAKENHI Grant Number 21H01811. H.T. acknowledges JST, the establishment of university fellowships towards the creation of science technology innovation, Grant Number JPMJFS2123.

Data Availability

The data that support the findings of this study are available from the corresponding author upon reasonable request.

References

- ¹ J.Y. Tsao, S. Chowdhury, M.A. Hollis, D. Jena, N.M. Johnson, K.A. Jones, R.J. Kaplar, S. Rajan, C.G. Van de Walle, E. Bellotti, C.L. Chua, R. Collazo, M.E. Coltrin, J.A. Cooper, K.R. Evans, S. Graham, T.A. Grotjohn, E.R. Heller, M. Higashiwaki, M.S. Islam, P.W. Juodawlkis, M.A. Khan, A.D. Koehler, J.H. Leach, U.K. Mishra, R.J. Nemanich, R.C.N. Pilawa-Podgurski, J.B. Shealy, Z. Sitar, M.J. Tadjer, A.F. Witulski, M. Wraback, and J.A. Simmons, *Adv. Electron. Mater.* **4**, 160051 (2018).
- ² M. Orita, H. Ohta, and M. Hirano, *Appl. Phys. Lett.* **77**, 4166 (2000).
- ³ T. Onuma, S. Saito, K. Sasaki, T. Masui, T. Yamaguchi, T. Honda, and M. Higashiwaki, *Jpn. J. Appl. Phys.* **54**, 112601 (2015).
- ⁴ M. Stapelbroek and B.D. Evans, *Solid State Commun.* **25**, 959 (1978).
- ⁵ S. Chae, J. Lee, K.A. Mengle, J.T. Heron, and E. Kioupakis, *Appl. Phys. Lett.* **114**, 102104 (2019).
- ⁶ K.A. Mengle, S. Chae, and E. Kioupakis, *J. Appl. Phys.* **126**, 085703 (2019).
- ⁷ C.A. Niedermeier, K. Ide, T. Katase, H. Hosono, and T. Kamiya, *J. Phys. Chem. C* **124**, 25721 (2020).
- ⁸ K. Bushick, K.A. Mengle, S. Chae, and E. Kioupakis, *Appl. Phys. Lett.* **117**, 182104 (2020).
- ⁹ S. Chae, K.A. Mengle, R. Lu, A. Olvera, N. Sanders, J. Lee, P.F.P. Poudeu, J.T. Heron, and E. Kioupakis, *Appl. Phys. Lett.* **117**, 102106 (2020).
- ¹⁰ J.W. Goodrum, *J. Cryst. Growth* **7**, 254 (1970).
- ¹¹ D.E. Swets, *J. Cryst. Growth* **8**, 311 (1971).

- ¹² V. Agafonov, D. Michel, M. Perez y Jorba, and M. Fedoroff, *Mater. Res. Bull.* **19**, 233 (1984).
- ¹³ S. Chae, H. Paik, N.M. Vu, E. Kioupakis, and J.T. Heron, *Appl. Phys. Lett.* **117**, 072105 (2020).
- ¹⁴ H. Takane and K. Kaneko, *Appl. Phys. Lett.* **119**, 062104 (2021).
- ¹⁵ G. Deng, K. Saito, T. Tanaka, M. Arita, and Q. Guo, *Appl. Phys. Lett.* **119**, 182101 (2021).
- ¹⁶ A. Sasaki, M. Nishiuma, and Y. Takeda, *Jpn. J. Appl. Phys.* **19**, 1695 (1980).
- ¹⁷ I. Akasaki and H. Amano, *Jpn. J. Appl. Phys.* **36**, 5393 (1997).
- ¹⁸ O. Ambacher, *J. Phys. D. Appl. Phys.* **31**, 2653 (1998).
- ¹⁹ K. Kaneko, T. Nomura, I. Kakeya, and S. Fujita, *Appl. Phys. Express* **2**, 075501 (2009).
- ²⁰ S. Fujita and K. Kaneko, *J. Cryst. Growth* **401**, 588 (2014).
- ²¹ D. Fröhlich, R. Kenkies, and R. Helbig, *Phys. Rev. Lett.* **41**, 1750 (1978).
- ²² T. Minami, *Semicond. Sci. Technol.* **20**, S35 (2005).
- ²³ W. Göpel and K.D. Schierbaum, *Sensors Actuators B* **26**, 1 (1995).
- ²⁴ T. Oshima, T. Okuno, and S. Fujita, *Jpn. J. Appl. Phys.* **48**, 120207 (2009).
- ²⁵ R.E. Presley, C.L. Munsee, C.H. Park, D. Hong, J.F. Wager, and D.A. Keszler, *J. Phys. D. Appl. Phys.* **37**, 2810 (2004).
- ²⁶ G.T. Dang, T. Uchida, T. Kawaharamura, M. Furuta, A.R. Hyndman, R. Martinez, S. Fujita, R.J. Reeves, and M.W. Allen, *Appl. Phys. Express* **9**, 041101 (2016).
- ²⁷ A.N. Trukhin, T.I. Dyuzheva, L.M. Lityagina, and N.A. Bendeliani, *Solid State Commun.* **131**, 1 (2004).
- ²⁸ J. Pascual, J. Camassel, and H. Mathieu, *Phys. Rev. B* **18**, 5606 (1978).
- ²⁹ W.H. Baur and A.A. Khan, *Acta Crystallogr. Sect. B* **27**, 2133 (1971).
- ³⁰ S. Fujita, *Jpn. J. Appl. Phys.* **54**, 030101 (2015).
- ³¹ P. Giannozzi, S. Baroni, N. Bonini, M. Calandra, R. Car, C. Cavazzoni, D. Ceresoli, G.L. Chiarotti, M. Cococcioni, I. Dabo, A.D. Corso, S. De Gironcoli, S. Fabris, G. Fratesi, R. Gebauer, U. Gerstmann, C. Gougoussis, A. Kokalj, M. Lazzeri, L. Martin-samos, N. Marzari, F. Mauri, R. Mazzarello, S. Paolini, A. Pasquarello, L. Paulatto, C. Sbraccia, A. Smogunov, P. Umari, and R.M. Wentzcovitch, *J. Phys. Condens. Matter* **21**, 395502 (2009).

- ³² P. Giannozzi, O. Andreussi, T. Brumme, O. Bunau, M.B. Nardelli, M. Calandra, R. Car, C. Cavazzoni, D. Ceresoli, M. Cococcioni, N. Colonna, I. Carnimeo, A.D. Corso, S. De Gironcoli, G. Delugas, R.A.D. Jr, A. Ferretti, A. Floris, G. Fratesi, G. Fugallo, R. Gebauer, U. Gerstmann, F. Giustino, T. Gorni, J. Jia, M. Kawamura, H.-Y. Ko, A. Kokalj, E. Küçükbenli, M. Lazzeri, M. Marsili, N. Marzari, F. Mauri, N.L. Nguyen, H.-V. Nguyen, A. Otero-de-la-Roza, L. Paulatto, S. Poncé, D. Rocca, R. Sabatini, B. Santra, M. Sclipf, A.P. Seitsonen, A. Smogunov, I. Timrov, T. Thonhauser, P. Umari, N. Vast, X. Wu, and S. Baroni, *J. Phys. Condens. Matter* **29**, 465901 (2017).
- ³³ P. Blaha, K. Schwarz, F. Tran, R. Laskowski, G.K.H. Madsen, and L.D. Marks, *J. Chem. Phys.* **152**, 074101 (2020).
- ³⁴ A.R. Oganov and C.W. Glass, *J. Chem. Phys.* **124**, 244704 (2006).
- ³⁵ A.O. Lyakhov, A.R. Oganov, H.T. Stokes, and Q. Zhu, *Comput. Phys. Commun.* **184**, 1172 (2013).
- ³⁶ A.R. Oganov, A.O. Lyakhov, and M. Valle, *Acc. Chem. Res.* **44**, 227 (2011).
- ³⁷ J.P. Perdew, A. Ruzsinszky, G.I. Csonka, O.A. Vydrov, G.E. Scuseria, L.A. Constantin, X. Zhou, and K. Burke, *Phys. Rev. Lett.* **100**, 136406 (2008).
- ³⁸ G. Prandini, A. Marrazzo, I.E. Castelli, N. Mounet, and N. Marzari, *npj Comput. Mater.* **4**, 72 (2018).
- ³⁹ H.J. Monkhorst and J.D. Pack, *Phys. Rev. B* **13**, 5188 (1976).
- ⁴⁰ J.P. Perdew, K. Burke, and M. Ernzerhof, *Phys. Rev. Lett.* **77**, 3865 (1996).
- ⁴¹ F. Tran and P. Blaha, *Phys. Rev. Lett.* **102**, 226401 (2009).
- ⁴² D. Koller, F. Tran, and P. Blaha, *Phys. Rev. B* **85**, 155109 (2012).
- ⁴³ Y. Ota, *AIP Adv.* **10**, 125321 (2020).
- ⁴⁴ B.D. Pelatt, J.F. Wager, and D.A. Keszler, *J. Solid State Chem.* **274**, 337 (2019).
- ⁴⁵ M. Fukumoto, S. Nakao, K. Shigematsu, D. Ogawa, K. Morikawa, Y. Hirose, and T. Hasegawa, *Sci. Rep.* **10**, 6844 (2020).
- ⁴⁶ H. Takane and K. Kaneko, *Appl. Phys. Lett.* **120**, 099903 (2022).
- ⁴⁷ R.K. Ham, *Philos. Mag.* **6**, 1183 (1961).
- ⁴⁸ G.E. Jellison and F.A. Modine, *Appl. Phys. Lett.* **69**, 371 (1996).
- ⁴⁹ H. Chen and W.Z. Shen, *Eur. Phys. J. B* **43**, 503 (2005).
- ⁵⁰ M. Nagasawa and S. Shionoya, *Phys. Rev. Lett.* **21**, 1070 (1968).

- ⁵¹ M. Nagasawa and S. Shionoya, *J. Phys. Soc. Japan* **30**, 1118 (1971).
- ⁵² J. Tauc, R. Grigorovici, and A. Vancu, *Phys. Status Solidi B* **15**, 627 (1996).
- ⁵³ E.A. Davis and N.F. Mott, *Philos. Mag.* **22**, 903 (1970).
- ⁵⁴ A.D. Becke, *J. Chem. Phys.* **98**, 1372 (1993).
- ⁵⁵ J.P. Perdew, M. Ernzerhof, and K. Burke, *J. Chem. Phys.* **105**, 9982 (1996).
- ⁵⁶ J. Heyd, G.E. Scuseria, and M. Ernzerhof, *J. Chem. Phys.* **118**, 8207 (2003).
- ⁵⁷ L. Hedin, *Phys. Rev.* **139**, A796 (1965).
- ⁵⁸ F. Aryasetiawan and O. Gunnarsson, *Reports Prog. Phys.* **61**, 237 (1998).
- ⁵⁹ Y. Kang, G. Kang, H.H. Nahm, S.H. Cho, Y.S. Park, and S. Han, *Phys. Rev. B* **89**, 165130 (2014).
- ⁶⁰ S.B. Zhang, S.H. Wei, and A. Zunger, *J. Appl. Phys.* **83**, 3192 (1998).
- ⁶¹ S.B. Zhang, S.H. Wei, and A. Zunger, *Phys. Rev. Lett.* **84**, 1232 (2000).
- ⁶² S.B. Zhang, *J. Phys. Condens. Matter* **14**, R881 (2002).
- ⁶³ A. Zunger, *Appl. Phys. Lett.* **83**, 57 (2003).
- ⁶⁴ J. Robertson and S.J. Clark, *Phys. Rev. B* **83**, 075205 (2011).
- ⁶⁵ W. Walukiewicz, *Appl. Phys. Lett.* **54**, 2094 (1989).
- ⁶⁶ W. Walukiewicz, *J. Cryst. Growth* **159**, 244 (1996).
- ⁶⁷ W. Walukiewicz, *Phys. B* **302–303**, 123 (2001).
- ⁶⁸ S.X. Li, K.M. Yu, J. Wu, R.E. Jones, W. Walukiewicz, J.W. Ager, W. Shan, E.E. Haller, H. Lu, and W.J. Schaff, *Phys. Rev. B* **71**, 161201(R) (2005).
- ⁶⁹ Ç. Kiliç and A. Zunger, *Appl. Phys. Lett.* **81**, 73 (2002).
- ⁷⁰ A.K. Singh, A. Janotti, M. Scheffler, and C.G. Van de Walle, *Phys. Rev. Lett.* **101**, 055502 (2008).
- ⁷¹ P.D.C. King, R.L. Lichti, Y.G. Celebi, J.M. Gil, R.C. Vilão, H. V. Alberto, J. Piroto Duarte, D.J. Payne, R.G. Egdell, I. McKenzie, C.F. McConville, S.F.J. Cox, and T.D. Veal, *Phys. Rev. B* **80**, 081201(R) (2009).
- ⁷² H. Ehrenreich, *J. Phys. Chem. Solids* **12**, 97 (1959).
- ⁷³ L. Makowski and M. Glicksman, *J. Phys. Chem. Solids* **34**, 487 (1973).
- ⁷⁴ J.W. Harrison and J.R. Hauser, *Phys. Rev. B* **13**, 5347 (1976).
- ⁷⁵ B. Russo and G.Z. Cao, *Appl. Phys. A Mater. Sci. Process.* **90**, 311 (2008).
- ⁷⁶ H. Iida, T. Mishuku, A. Ito, K. Kato, M. Yamanaka, and Y. Hayashi, *Sol. Energy Mater.*

17, 407 (1988).